5154 *Chem. Mater.* **2009,** *21,* 5154–5162
DOI:10.1021/cm902094q

CHEMISTRY OF MATERIALS
Article

B Cation Ordered Double Perovskite $Ba_2CoMo_{0.5}Nb_{0.5}O_{6-\delta}$ As a Potential SOFC Cathode

Z.Q. Deng, J.P. Smit, H.J. Niu, G. Evans, M.R. Li, Z.L. Xu, J.B. Claridge, and M.J. Rosseinsky*

Department of Chemistry, The University of Liverpool, Liverpool L69 7ZD, United Kingdom

Received July 10, 2009. Revised Manuscript Received August 19, 2009

This paper reports the evaluation of the cubic B site cation-ordered double perovskite system $Ba_2Co_{2-x}(Mo_{1/2}Nb_{1/2})_xO_6$, resulting in the single phase composition $Ba_2CoMo_{0.5}Nb_{0.5}O_{6-\delta}$ (BCMN) with a mixed Co charge state stabilized by a combination of Mo and Nb doping as a new mixed conductor with potential SOFC cathode applications. X-ray, neutron, and electron diffraction show that hexagonal intergrowths found in multiple phase samples at lower Mo/Nb contents are suppressed in BCMN, which has large domains of rock-salt ordered B site cations with separate Co and Mo/Nb sites. Conductivity measurement and impedance spectroscopy investigation shows that BCMN has a considerably reduced dc conductivity compared with materials such as BSCF but exhibits comparable electrochemical properties to some existing cathode materials in symmetrical cell measurements, and shows higher structural stability and reduced reactivity with the $Ce_{0.8}Sm_{0.2}O_{2-\delta}$ (SDC) electrolyte. The role of Mo in dioxygen activation is proposed to offset the reduction that the d^0 Mo(VI) and Nb(V) cations on the B site produce in the electronic and ionic conductivity.

Introduction

With increasing demand for clean and renewable energy, solid-oxide fuel cells (SOFCs) have received much attention because of their energy efficiency, environmental friendliness and excellent fuel flexibility in comparison with other fuel cell types. To make SOFCs economically competitive with the existing technology, an intermediate temperature operating range of 500−750 °C is needed.[1−4] This remains a challenge because of a lack of appropriate SOFC component materials to compensate for the significant increase in electrolyte and electrode ohmic and polarization losses at lower temperatures. Electrolytes overcome this barrier with higher ionic conductivity and/or decreased thickness, such as Gd^{3+}- or Sm^{3+}-doped CeO_2, Sr^{2+}- and Mg^{2+}-doped $LaGaO_3$ (LSGM), whereas the anode could be either a cermet of Ni and yttria-stabilized zirconia (YSZ) or doped CeO_2.[5] Therefore, the largest contribution to the total resistance at decreased operating temperatures is the cathodic polarization resistance, associated particularly with the kinetics of oxygen reduction, making the development of new cathode materials critical for SOFC commercialization.[6] With a target power density of 1 W cm^{-2}, the combined area-specific resistance (ASR) of the cell components (electrolyte, anode, and cathode) needs to be below 0.3 Ω cm^2, and ideally to approach 0.1 Ω cm^2.[1,2]

Early explorations of SOFC cathodes encompass perovskite-type and related structures. These materials combine high defect tolerance for oxygen vacancy ionic charge carriers, strong metal−oxygen−metal covalent overlap to give the band widths required for electronic conductivity and a range of octahedral-related sites to accommodate catalytically active transition metals for oxygen reduction. For example, $La_{1-x}Sr_xMnO_{3-\delta}$ (LSM with $x = 0.2$) is the present cathode choice for zirconia electrolyte-based SOFCs that operate efficiently at high temperatures (usually above 700 °C). Additionally, $Ln_{1-x}Sr_xCoO_{3-\delta}$ (Ln = La, LSC with $x = 0.4$, Ln = Sm, SSC with $x = 0.5$), $La_{1-x}Sr_xCo_{1-y}Fe_yO_{3-\delta}$ (LSCF with $x = 0.4$ and $y = 0.8$) and $Ba_{0.5}Sr_{0.5}Co_{0.8}Fe_{0.2}O_{3-\delta}$ (BSCF) have demonstrated promising performances with ceria electrolytes in the intermediate temperature range.[7−9] Alternative cathode materials have oxygen interstitial charge carriers, such as $LnBaCo_2O_{5+\delta}$ (Ln = Gd, Pr) with ordered A-site cations in the perovskite structure,[10] and the $n = 1$ Ruddlesden−Popper (RP) analogue $La_2NiO_{4+\delta}$.[11] The RP structure, which includes the

*Corresponding author.

(1) Steele, B. C. H.; Heinzel, A. *Nature* **2001**, *414*, 345.
(2) Vohs, J. M.; Gorte, R. J. *Adv. Mater.* **2009**, *21*, 943.
(3) Yang, L.; Zuo, C. D.; Wang, S. Z.; Cheng, Z.; Liu, M. L. *Adv. Mater.* **2008**, *20*, 3280.
(4) Brandon, N. P.; Skinner, S.; Steele, B. C. H. *Annu. Rev. Mater. Res.* **2003**, *33*, 183.
(5) Atkinson, A.; Barnett, S.; Gorte, R. J.; Irvine, J. T. S.; Mcevoy, A. J.; Mogensen, M.; Singhal, S. C.; Vohs, J. *Nat. Mater.* **2004**, *3*, 17.
(6) Ivers-Tiffée, E.; Weber, A.; Herbstritt, D. *J. Eur. Ceram. Soc.* **2001**, *21*, 1805.
(7) Shao, Z. P.; Haile, S. M. *Nature* **2004**, *431*, 170.
(8) Xia, C. R.; Rauch, W.; Chen, F. L.; Liu, M. L. *Solid State Ionics* **2002**, *149*, 11.
(9) Stevenson, J. W.; Armstrong, T. R.; Carneim, R. D.; Pederson, L. R.; Weber, W. J. *J. Electrochem. Soc.* **1996**, *143*, 2722.
(10) Tarancón, A.; Skinner, S. J.; Chater, R. J.; Ramirez, F. H.; Kilner, J. A. *J. Mater. Chem.* **2007**, *17*, 3175.
(11) Dong, X.; Wu, Z.; Chang, X.; Jin, W.; Xu, N. *Ind. Eng. Chem. Res.* **2007**, *46*, 6910.

 Published on Web 10/12/2009

phases $Sm_{0.5}Sr_{1.5}CoO_{4-\delta}$[12] and $LaSr_3(Fe,Co)_3O_{10-\delta}$,[13] is a layered analogue of the 3D vacancy-containing perovskites.[14] Mixed conducting materials of these types also have a wide range of applications in gas separation and catalytic reaction membranes.

Cobalt is often included in mixed-conducting perovskite oxides, as it gives rise to high electronic conductivity from strong covalency with oxygen, resulting from its position to the right of the first transition series, combined with the high metal oxidation states that are accessible. The production of oxygen vacancies, and thereby ionic conductivity at high temperature, is facilitated by the difficulty of attaining pure Co^{4+} in the cubic perovskite structure. One of the problems with perovskite cobaltites is the stability of competing hexagonal phases at high ($>+3$) cobalt oxidation states.

These hexagonal phases can produce degradation over time and disrupt promising performance as oxygen permeation membranes or SOFC cathodes. Another problem is the ordering of oxygen vacancies that has been demonstrated to occur in $Ln_{1-x}Sr_xCoO_{3-\delta}$ and $Sr_{0.8}Co_{0.8}Fe_{0.2}O_{3-\delta}$ below 750 °C at pO_2 below 0.1 atm, yielding an orthorhombic brownmillerite phase[15−17] and producing a significant decrease in electronic and ionic conductivity, in addition to mechanical instability associated with the lattice expansion. Partial substitution of Ba for Sr suppresses this type of transition, and indeed $Ba_{0.5}Sr_{0.5}Co_{0.8}Fe_{0.2}O_{3-\delta}$ has been reported among the most promising oxygen permeable membrane and SOFC cathode materials.[7] However, recent studies have shown the cubic perovskite phase undergoes decomposition into a hexagonal perovskite phase and a cubic perovskite phase at intermediate temperatures over time.[18] Interfacial reaction between the cathode and the electrolyte is another concern for the cathode performance. The stabilization of Co-containing cubic perovskites with retention of ionic and electronic conductivity is thus an important challenge.

Molybdenum compounds, such as $Ni_{0.5}Co_{0.5}MoO_4$, are well-known catalysts with high activity for selective oxidation of hydrocarbons, where the activation of oxygen by dissociation into reactive species is a key part of the catalyst function.[19,20] Niobium substitution has been found effective in the stabilization of the highly oxygen permeable cubic perovskite structure of strontium cobaltite.[21] This paper reports the evaluation of the perovskite system $Ba_2Co_{2-x}(Mo_{1/2}Nb_{1/2})_xO_6$ where cobalt, molybdenum and niobium are all present on the octahedral B site. This produces the cubic B site cation-ordered $x=1$ composition $Ba_2CoMo_{0.5}Nb_{0.5}O_{6-\delta}$ (BCMN) with a mixed Co charge state stabilized by a combination of Mo and Nb doping as a new mixed conductor. BCMN exhibits comparable electrochemical properties to some existing cathode materials, but with higher structural stability.

Experimental Section

Preparation of BCMN Samples. The $x=0.5$ $Ba_2Co_{1.5}Mo_{0.25}Nb_{0.25}O_{6-\delta}$ and $x=1$ $Ba_2CoMo_{0.5}Nb_{0.5}O_{6-\delta}$ (BCMN) members of the $Ba_2Co_{2-x}(Mo_{1/2}Nb_{1/2})_xO_6$ solid solution are reported in detail here. Materials were prepared via solid-state reaction. Stoichiometric amounts of high purity (99.99%) $BaCO_3$, Co_3O_4, MoO_3 and Nb_2O_5 were mixed together by ball milling for 24 h with alcohol, followed by drying, grinding, and calcination at 700 °C for 6 h and at 900 °C for 8 h. $Ba_{0.5}Sr_{0.5}Co_{0.8}Fe_{0.2}O_{3-\delta}$ (BSCF) was prepared using high purity (99.99%) $BaCO_3$, $SrCO_3$, Co_2O_3, and Fe_3O_4, which were ball-milled and subsequently calcined at 700 °C for 5 h, at 900 °C for 6 h and 1150 °C for 8 h in air. The resulting powders were then ball milled again, and isostatically pressed into pellets with an autoclave engineers cold isostatic press under a pressure of 200 MPa and subsequently sintered in air at 1100 °C for 12 h. After confirming a single phase was formed by X-ray diffraction (XRD), the pellets were cut into bars for the electrical conductivity measurement with standard d.c. four-probe method, using Keithley 2182 Nanovoltmeter and Keithley 220 Programmable Current Source, in which Pt paste and Pt wire were used to make the four probes with a four-in-a-line contact geometry, or crushed and ball milled again to produce powders for further characterization.

Characterization of Structure. The structure of the materials was analyzed by powder X-ray diffraction (PXRD) on a Panalytical X'pert Pro diffractometer (with Co $K_{\alpha 1}$ radiation). Time-of-flight neutron diffraction (ND) data were collected from room temperature to 900 °C at an interval of 100 °C on the POLARIS instrument at the ISIS facility, Rutherford Appleton Laboratories. The transmission electron microscopy (TEM) study was carried out on a JEOL JEM3010 (JEOL, LaB_6 filament, 300 keV) and energy-dispersive X-ray spectroscopy (EDX) data were collected on a JEM2000FX (JEOL, W filament, 200 keV). X-ray absorption near edge spectroscopy (XANES) was carried out in transmission mode in station 9.3 at the SRS synchrotron at Daresbury Laboratory (Warrington, UK).

Chemical Compatibility with SDC and Long-Term Annealing. The phase composition of the mixture of BCMN or BSCF with SDC powder ($Ce_{0.8}Sm_{0.2}O_{2-\delta}$, from fuelcellmaterials.com, surface area: 30−40 m^2/g, Particle Size (d50): 0.3 to 0.5 μm) calcined at different temperatures was determined by XRD. Powders of BCMN or BSCF and SDC with a weight ratio of 1:1 were well mixed, pressed into pellets and calcined at 1000 or 1050 °C for 5 or 10 h. The pellets were then crushed to powders for XRD characterization. For long-term structural stability tests, the as-synthesized single-phase powders of BCMN or BSCF were annealed at 750 °C in air for 240 h, then characterized by XRD.

Symmetric Cell Fabrication and Testing. SDC was first pressed into pellets and then sintered at 1400 °C for 8 h to obtain fully dense SDC electrolyte substrates (1.5 mm thick, 10 mm diameter). To prepare the electrode paste, we mixed BCMN powders by ball milling with an organic binder (Heraeus V006) and thinner (Heraeus RV372). The electrode pastes were applied onto both surfaces of the SDC substrates by screen printing and then sintered in air at 1000 °C for 3 h. The thickness and

(12) Wang, Y. S.; Nie, H. W.; Wang, S. R.; Wen, T. L.; Guth, U.; Valshook, V. *Mater. Lett.* **2006**, *60*, 1174.
(13) Lee, K. T.; Manthiram, A. *Chem. Mater.* **2006**, *18*, 1621.
(14) Boehm, E.; Bassat, J. M.; Steil, M. C.; Dordor, P.; Mauvy, F.; Grenier, J. C. *Solid State Sci.* **2003**, *5*, 973.
(15) Kruidhof, H.; Bouwmeester, H. J. M.; Doorn, R. H. E. v.; Burggraaf, A. J. *Solid State Ionics* **1993**, *63−65*, 816.
(16) Deng, Z. Q.; Yang, W. S.; Liu, W.; Chen, C. S. *J. Solid State Chem.* **2006**, *179*, 362.
(17) Harrison, W. T. A.; Lee, T. H.; Yang, Y. L.; Scarpe, D. P.; Liu, L. M.; Jacobson, A. J. *Mater. Res. Bull.* **1995**, *30*, 621.
(18) Švarcová, S.; Wiik, K.; Tolchard, J.; Bouwmeester, H. J. M.; Grande, T. *Solid State Ionics* **2008**, *178*, 1787.
(19) Stern, D. L; Grasselli, R. K. *J. Catal.* **1997**, *167*, 550.
(20) Yoon, Y. S.; Ueda, W.; Moro-ok, Y. *Top. Catal.* **1996**, *3*, 265.
(21) Nagai, T.; Ito, W.; Sakon, T. *Solid State Ionics* **2007**, *177*, 3433.

diameter of the electrodes are about 30 μm and 10 mm, respectively. The contacts for the electrical measurements were made using gold mesh fixed with gold paste. The impedance spectra of the symmetric cells were measured under an air atmosphere with a flow rate of 100 mL/min in the range from 550 to 800 °C, using a Solartron 1260 frequency response analyzer coupled to a Solartron 1287 electrochemical interface and controlled by ZPlot electrochemical impedance software. The impedance spectra were analyzed with the Zview software (Scribner Associates, Inc.). The measurements were repeated on a second cell prepared with the same process. The microstructure of the electrodes was investigated by scanning electron microscopy using a Hitachi S4800 type II cold field emission scanning electron microscope. The samples were observed using a mix of upper and lower secondary electron detectors operating at an acceleration voltage of 3 kV with a working distance of 8.0 mm.

Results

Composition and Structure. The results of the solid state syntheses were initially assessed by PXRD which revealed the temperature ranges required for phase formation and the compositional limits for the cubic perovskite phase within the $Ba_2Co_{2-x}(Mo_{1/2}Nb_{1/2})_xO_6$ family. The only single phase composition produced under the reaction conditions studied is $x = 1$ $Ba_2CoMo_{0.5}Nb_{0.5}O_6$, where the EDX-determined atomic ratios of Ba, Co, Mo and Nb are 2.02:1.01:0.48:0.49, close to the nominal composition. Substitutions to enhance the Co content further (exemplified here by $x = 0.5$, $Ba_2Co_{1.5}Mo_{0.25}Nb_{0.25}O_{6-\delta}$) produce multiple phase systems discussed later after the single phase material. The ND, XANES, selected area electron diffraction (SAED), and high resolution TEM (HRTEM) results (Figures 1-4) for the single phase $x = 1$ composition $Ba_2CoMo_{0.5}Nb_{0.5}O_{6-\delta}$ (BCMN) show that it adopts a B site ordered double perovskite structure, $A_2B'B''O_6$ (space group $Fm\bar{3}m$), with A = Ba at the 8*c* site, B' = Co at the 4*a* site, and B'' = $Mo_{0.5}Nb_{0.5}$ at the 4*b* site at both room and high temperatures.[22] Here, the ND data were used to refine the oxygen content and the occupancy fraction for the B site cations in the rock salt arrangement, with the constraints of nominal compositions and identical atomic displacement parameter values set for Mo and Nb. The B-site cationic antisite disorder was examined by introducing Co/(Mo,Nb), Co/Mo, or Co/Nb disorder. The best refinement results come from the Co/(Mo,Nb) antisite disorder (where antisite disorder y between the 4*a* Co and 4*b* Mo/Nb positions disorders an equal amount of Mo and Nb) with a formula of $Ba_2(Co_{1-y}Mo_{y/2}Nb_{y/2})(Mo_{0.5-y/2}Nb_{0.5-y/2}Co_y)O_{6-\delta}$. Refinement affords $y = 0.10(1)$ ($\chi^2 = 1.57$, $R_F^2 = 6.55\%$) at room temperature and $y = 0.07$ (1) ($\chi^2 = 1.43$, $R_F^2 = 14.23\%$) at 900 °C. The final refined structural results for $Ba_2CoMo_{0.5}Nb_{0.5}O_{6-\delta}$ at room temperature and 900 °C are shown in Figures 1 and S1−S4 and Tables 1 and S1−S4.

XANES spectra (Figure 2) show Nb is present as Nb^{5+}, with a mixed oxidation state of +2/+3 for Co at room temperature (RT). Quantitative analysis of the XANES

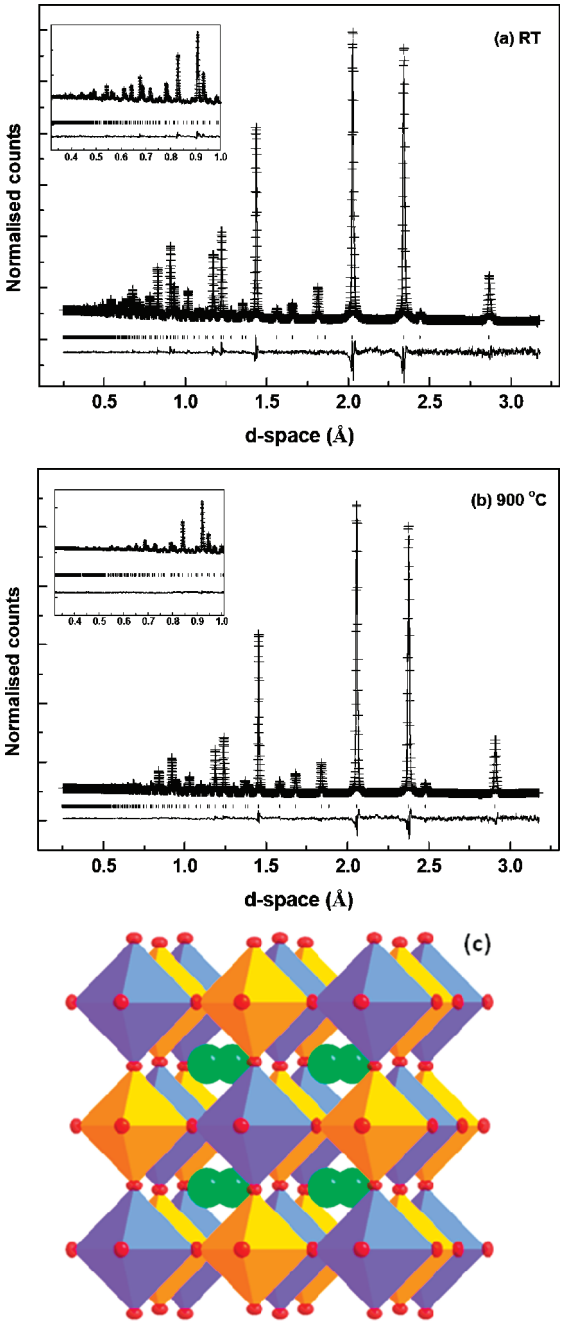

Figure 1. Rietveld refinement of neutron powder diffraction data from (a) room temperature, (b) 900 °C for $Ba_2CoMo_{0.5}Nb_{0.5}O_{6-\delta}$. The upper tick marks indicate the location of individual Bragg reflections. The lower curve is the difference plot between the observed and calculated profiles. (Inset shows the low *d*-space data). (c) Unit-cell polyhedral structure of $Ba_2CoMo_{0.5}Nb_{0.5}O_{6-\delta}$ (BCMN) at 900 °C from the Co/(Mo,Nb) antisite disordering model (Table 1), showing the rock salt arrangement of B site cations and the atomic displacement parameters of O (90% weighted). Ba, green; O, red; $[Co_{0.93}(Mo_{0.5}Nb_{0.5})_{0.07}]O_6$ octahedron, blue; $[(Mo_{0.5}Nb_{0.5})_{0.93}Co_{0.07}]O_6$ octahedron, orange. Figure S5 in the Supporting Information is a representation of the structure at both temperatures where all ADPs are shown.

data by the shift in the edge position compared to the reference samples (NdSr)CoO_4 and La_2CoO_4 reveals a ratio of 70:30 for Co^{2+}:Co^{3+} i.e., a mean Co oxidation state of +2.3.[23] The oxide chemistry of Mo indicates the formation of Mo(VI) as does the formation of Nb(V)

(22) Kobayashi, K. I.; Kimura, T.; Sawada, H.; Terakura, K.; Tokura, Y. *Nature* **1998**, *395*, 677.

(23) Arcon, I.; Mirtic, B.; Kodre, A. *J. Am. Ceram. Soc.* **1998**, *81*, 222.

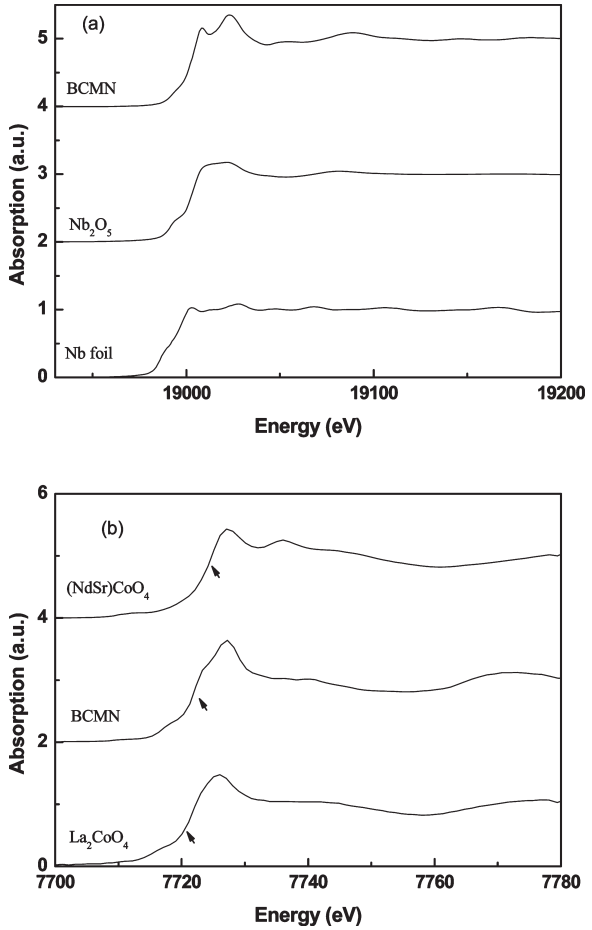

Figure 2. (a) Nb K-edge and (b) Co K-edge XANES spectra of $Ba_2CoMo_{0.5}Nb_{0.5}O_{6-\delta}$ (BCMN) with the oxidation state standards described in the text. The arrow indicates the inflection point, which is taken as the energy position of the edge.

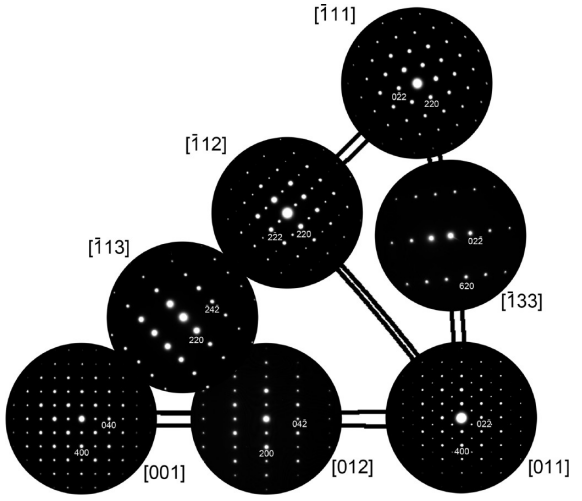

Figure 3. Composite SAED patterns of [001], [011], [012],[$\bar{1}$11],[$\bar{1}$33], [$\bar{1}$12], and [$\bar{1}$13] zone axes for $Ba_2CoMo_{0.5}Nb_{0.5}O_{6-\delta}$. The diffraction patterns are indexed according to a double perovskite cubic unit cell with lattice parameters $a \approx 8.1$ Å and space group $Fm\bar{3}m$.

under the synthesis conditions.[24] The oxygen content calculated from this charge distribution is 5.90, which agrees well with the value obtained from neutron refinement, 5.87(7) at room temperature. The change of refined oxygen content between RT and 900 °C is 0.17 per formula unit, which is comparable to oxygen loss evaluated from TGA in air (0.14 per formula unit), suggesting the reduction of Co^{3+} to 5.90, which agrees well with the value obtained from neutron refinement, 5.87(7) at room temperature. The change of refined oxygen content between RT and 900 °C is 0.17 per formula unit, which is comparable to oxygen loss evaluated from thermogravimetric analysis (TGA) in air (0.14 per formula unit), suggesting the reduction of Co^{3+} to Co^{2+} at high temperatures with a Co charge state close to +2. The refined change in cation antisite disorder on heating is at the 3σ level—if such a change is present, it may relate to the change in coordination number at the B sites locally affected by the change in oxygen occupancy indicated by both TGA and neutron diffraction. Variable temperature ND data (see Figure S5 in the Supporting Information) allows determination of the lattice expansion coefficient of BCMN and gives 14.3 and 18.7 ppm K^{-1} between 100 and 400 °C and 600−900 °C respectively. The average value of 16.0 ppm K^{-1} for BCMN is almost identical to LSCF and lower than BSCF (27.3 ppm K^{-1} for BSCF and 16.2 ppm K^{-1} for $La_{0.6}Sr_{0.4}Co_{0.2}Fe_{0.8}O_{3-\delta}$)[25] while still higher than that of SDC (12.7 ppm K^{-1}) in the temperature range 20−900 °C. Both thermal and chemical expansion due to the observed oxygen nonstoichiometry, as reported in LSCF[26] and BSCF,[27] are expected to contribute to the lattice expansion effect.

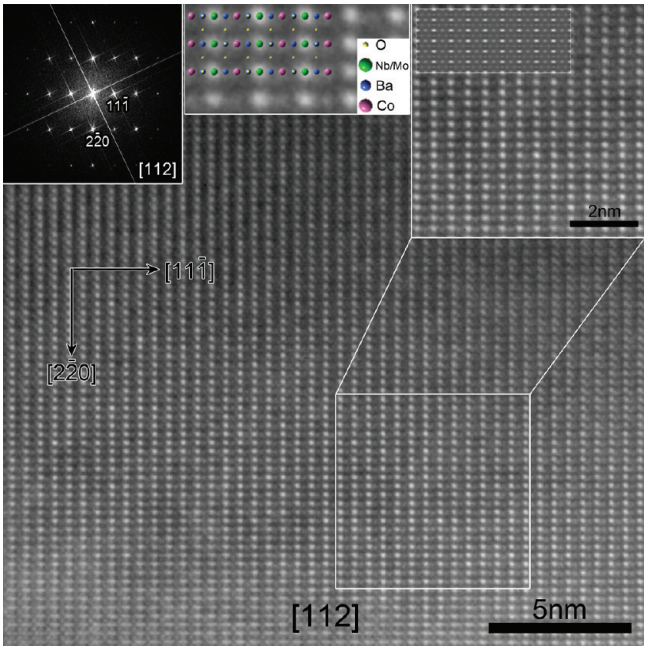

Figure 4. HRTEM along the [112] zone axis for $Ba_2CoMo_{0.5}Nb_{0.5}O_{6-\delta}$. The insets from top left to right are FFT patterns of the image, schematic drawing of the atomic projection according to the HRTEM simulation, and details of the framed area with simulated image, respectively.

(24) Deng, Z. Q.; Niu, H. J.; Kuang, X. J.; Allix, M.; Claridge, J. B.; Rosseinsky, M. J. *Chem. Mater.* **2008**, *20*, 6911.
(25) Ried, P.; Holtappels, P.; Wichser, A.; Ulrich, A.; Graule, T. *J. Electrochem. Soc.* **2008**, *155*, B1029.
(26) Adler, S. B. *J. Am. Ceram. Soc.* **2001**, *84*, 2117.
(27) McIntosh, S.; Vente, J. F.; Haije, W. G.; Blank, D. H. A.; Bouwmeester, H. J. M. *Chem. Mater.* **2006**, *18*, 2187.

Table 1. Refined Structural Parameters for $Ba_2CoMo_{0.5}Nb_{0.5}O_{6-\delta}$ from Neutron Diffraction Data (space group $Fm\bar{3}m$) at Room Temperature (RT) and 900 °C

	RT	900 °C
a (Å)	8.10728(6)	8.22272(4)
Ba, 8c, 0.25, 0.25, 0.25, U_{iso} (Å^2)	0.0055(2)	0.0227(3)
Co/(Mo,Nb), 4a, 0, 0, 0, U_{iso} (Å^2)[a]	0.0071(9)	0.0246(14)
occupancy	0.897(12)/0.051(6)/0.051(6)	0.930(10)/0.035(5)/0.035(5)
Mo/Nb/Co[a], 4b, 0.5, 0, 0, U_{iso} (Å^2)[a]	0.0031(3)	0.0130(5)
occupancy	0.449(6)/0.449(6)/0.102(12)	0.465(5)/0.465(5)/0.070(10)
O, 24e, x, 0, 0 U_{anis} (Å^2)[b]	0.2579(2)	0.2589(2)
U_{11}	0.0082(4)	0.0175(5)
$U_{22} = U_{33}$	0.0083(2)	0.0321(3)
occupancy	0.979(5)	0.950(4)
oxygen content per formula	$O_{5.87(7)}$	$O_{5.70(2)}$
R_p(%)/R_{wp}(%)/χ^2/R_F^2(%)	2.25/4.85/1.57/6.55	1.10/2.57/1.43/14.23

[a] U_{iso} of mixed site atoms were constrained to be the same. [b] $U_{ij} = 0$.

TEM studies were undertaken to check the local crystal structure. The seven major SAED patterns (Figure 3), particularly the presence of {111} diffraction in the [$\bar{1}$12] and [011] zone axis patterns, confirm that BCMN has a double perovskite cubic unit cell with lattice parameters $a \approx 8.1$ Å and that the reflection conditions correspond to space group $Fm\bar{3}m$, consistent with B site cation order. Many SAEDs along other zone axes and from different grains were taken and indexed well on the same cell, with no extra weak diffraction or streaking apparent, indicating that the average B site cation order probed by neutron diffraction is maintained on shorter length scales. The B site cation ordering is confirmed by an HRTEM image along the [112] zone axis (Figure 4), a direction from which the neighboring B sites can be readily separated. Along the [11$\bar{1}$] direction, the B layers are stacked with alternate black and white contrast, which means the B sites are alternately occupied by different cations. The HRTEM image simulation showed that darker B layers are occupied by Co while the brighter B layers are occupied by Mo/Nb. The cation ordered domain size was evaluated (with the Scherrer formula) by using fitted individual peak parameters, giving an average crystallite/diffracting region size of 75 nm from even reflections ($hkl = 2n$), and an average cation-ordered domain size of 66 nm from odd reflections ($hkl = 2n+1$).

X-ray powder diffraction data from the higher Co content $x = 0.5$ sample $Ba_2Co_{2-x}(Mo_{1/2}Nb_{1/2})_xO_6$ can only be fitted with two simple cubic perovskite phases (see Figure S6 in the Supporting Information). Consistent with this absence of the B site cation order found at $x = 1$, an SAED study proved that most of the particles have the simple cubic perovskite structure with a lattice parameter of about 4 Å. Very weak streaks along {111} in the [011] and [$\bar{1}$12] diffraction pattern were regularly observed. HRTEM described later leads to the interpretation of this scattering as arising from stacking faults along {111}. There are relatively high intensities where the diffuse streaks cross at ((2n + 1)/2){111} in [011] (see Figure S7 in the Supporting Information), which could be interpreted as B site cation ordering. However, because no such intensity is observed at the equivalent points in the [$\bar{1}$12] pattern, these intensities are assigned to the overlap of stacking fault-derived scattering rather than to B site cation order.

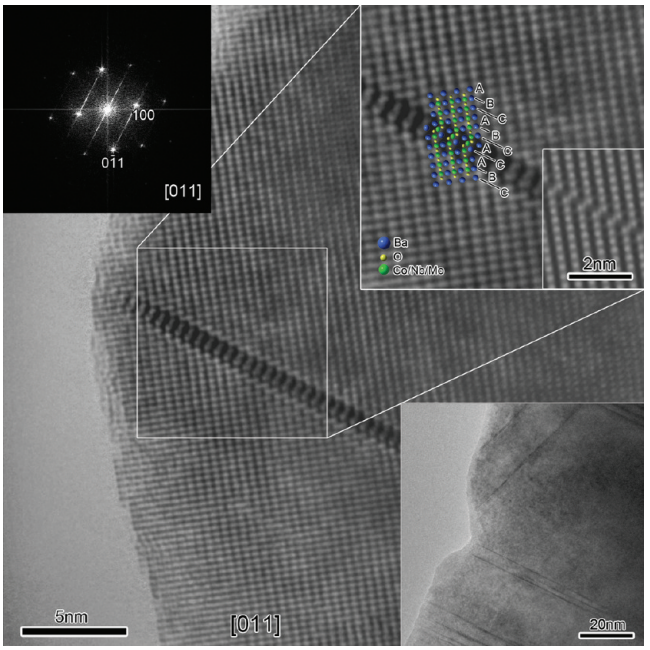

Figure 5. HRTEM along the [011] zone axis for $x = 0.5$ $Ba_2Co_{1.5}Mo_{0.25}Nb_{0.25}O_6$. The insets from top left to bottom right are the FFT pattern of the image, details of the framed area with the simulated image and atomic model used in the simulation, and a low magnification TEM image showing stacking faults along equivalent ⟨111⟩ directions, respectively.

The HRTEM viewed along the [011] axis reveals stacking faults in the (11$\bar{1}$) and (1$\bar{1}$1) (bottom right inset) planes in the same grain. In the defect free area of the crystal, {111} BaO_3 close-packed planes are arranged in the cubic perovskite ...ABCABC...sequence. According to the proposed atomic model of the defect, the stacking faults arise from conversion of a BaO_3 (11$\bar{1}$) plane (B in the Figure 5) into a hexagonally stacked C component in an ACA sequence, representing intergrowth of a $BaCoO_3$-type hexagonal perovskite in the cubic sequence. This is consistent with the streaking observed along [11$\bar{1}$] in the fast Fourier transform (FFT) pattern (top left inset) of the HRTEM, whereas no visible intensity associated with cation ordering is found at ((2n + 1)/2){111} in the FFT of perfect areas, which directly confirmed the SAED analysis. This stacking fault is widely observed in the sample, and its densities are different from particle to particle,

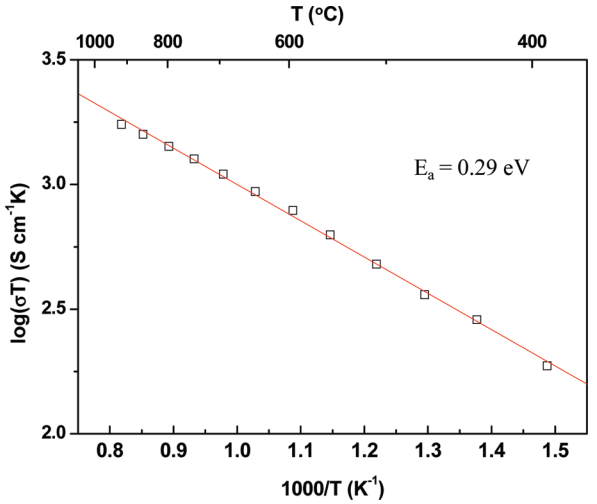

Figure 6. Temperature dependence of the dc electrical conductivity for $Ba_2CoMo_{0.5}Nb_{0.5}O_{6-\delta}$ samples in air.

hence the long-range XRD only shows the cubic matrix material. Electrical and electrochemical characterization was thus carried out solely on the single phase $x = 1$ material.

Electrical Properties and Symmetrical Electrochemical Cells. Processing of the BCMN powder affords ceramics of ~90% density. Four-probe d.c. electrical conductivity data (Figure 6) were measured in air on these samples over the temperature range 400−950 °C. $Ba_2CoMo_{0.5}Nb_{0.5}O_{6-\delta}$ exhibits an electrical conductivity of 1.2 and 1.0 S cm^{-1} at 800 and 700 °C, respectively, with an activation energy of 0.29 eV over the measured temperature range. For comparison, the electrical conductivity measured in our lab for BSCF (of ~90% density, comparable to that of the BCMN studied here) is 38−43 S/cm over 600 to 800 °C, also in good agreement with previous reports.[7]

Figure 7a shows a typical cross-sectional scanning electron microscope (SEM) image of the fractured electrolyte/electrode bilayer of the symmetrical BCMN/SDC/BCMN cell fabricated by a screen-printing technique, sintered at 1000 °C for 3 h. The BCMN electrode presents the required highly porous morphology; with a homogeneous thickness of 28−30 μm (the Au current collector is also seen on the electrode top). The image also indicates that the SDC electrolyte has a fully dense structure, and good adhesion to the electrode. A representative surface SEM image, Figure 7b, reveals a uniform and porous electrode structure formed by BCMN oxide grains with an average size of 500 nm and good intergrain connection.

Impedance spectroscopy measurements (Figure 8) were performed on the symmetrical BCMN/SDC/BCMN cell shown in Figure 7 over the temperature range 550−800 °C in air. The difference between the low-frequency (LF) and the high-frequency (HF) intercepts on the real axis is taken as the area specific resistance (ASR). The measured values for the pure BCMN cathode were 0.09, 0.20, 0.49, and 1.31 Ω cm^2 at 750, 700, 650, and 600 °C, respectively.

For direct comparison, the ASR of a symmetric cell BSCF/SDC/BSCF, fabricated in a manner identical to that

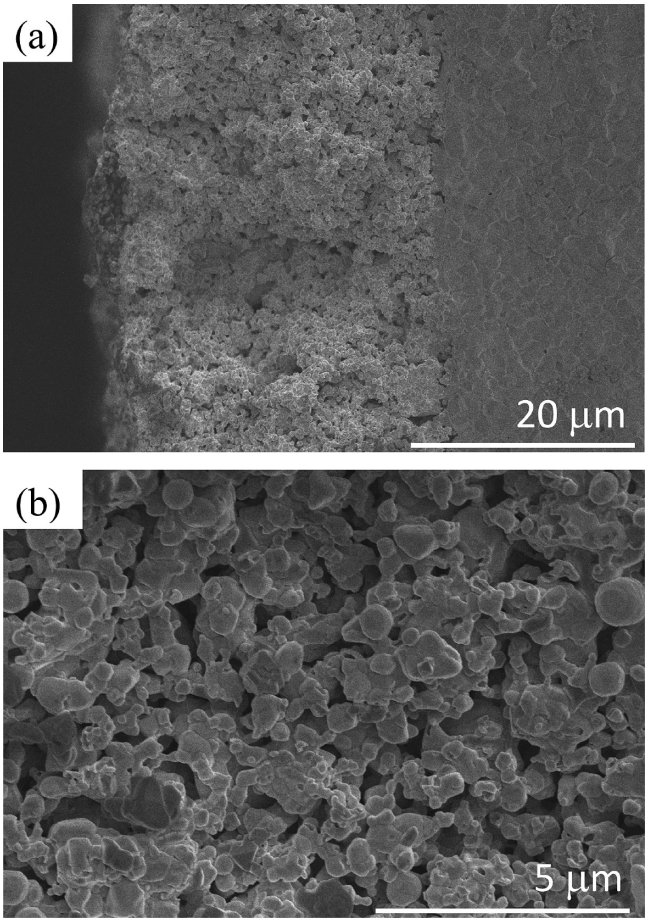

Figure 7. SEM images of (a) cross-sectional and (b) surface views of the $Ba_2CoMo_{0.5}Nb_{0.5}O_{6-\delta}$ cathode with SDC electrolyte in a symmetrical cell configuration fired at 1000 °C for 3 h.

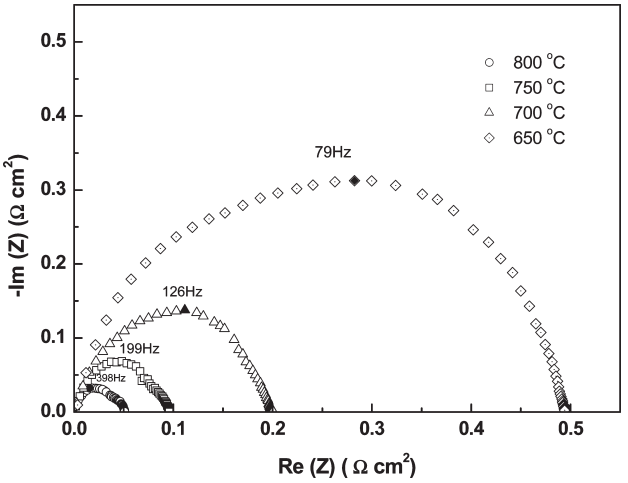

Figure 8. Cathode polarization of $Ba_2CoMo_{0.5}Nb_{0.5}O_{6-\delta}$ on an SDC electrolyte symmetric cell measured in air at 800, 750, 700, and 650 °C. The electrolyte contribution has been subtracted from the overall resistance, which is the cell resistance divided by two and represents the polarization of one electrode.

used for cells containing BCMN as the cathode in this study (except the cell was sintered at a slightly lower temperature of 970 °C for 3 h because of reactions between BSCF and SDC which occur at temperatures where BCMN is stable, as shown below), was measured. An ASR value of 0.51 Ω cm^2

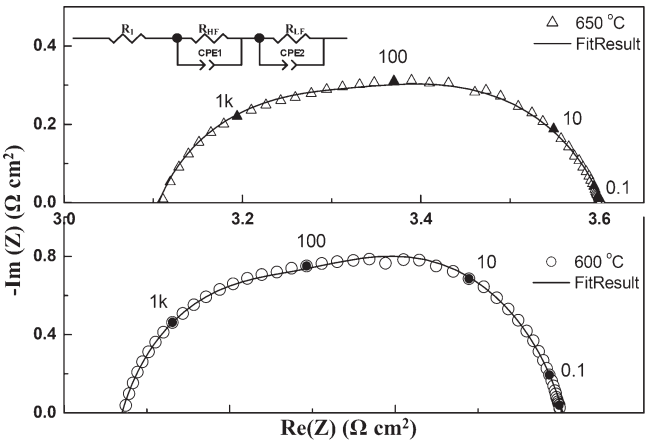

Figure 9. Fitting the impedance spectra of $Ba_2CoMo_{0.5}Nb_{0.5}O_{6-\delta}$/SDC/$Ba_2CoMo_{0.5}Nb_{0.5}O_{6-\delta}$ at (a) 650 and (b) 600 °C to the equivalent circuit shown in the insert. R_1 is the overall ohmic resistance, R_{HF} and R_{LF} correspond to the high and low frequency resistance arcs from the electrode, respectively, and CPE is a constant phase element.

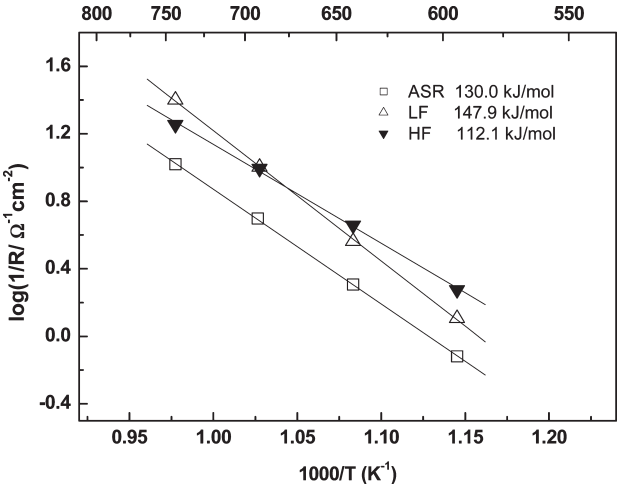

Figure 10. Activation energy for the high and low frequency resistance elements and the total ASR from the $Ba_2CoMo_{0.5}Nb_{0.5}O_{6-\delta}$ /SDC/$Ba_2CoMo_{0.5}Nb_{0.5}O_{6-\delta}$ cell in the temperature range 600 °C-750 °C.

was observed at 600 °C, which is in good agreement with prior reports and a factor of ~2.5 lower than that observed for the present BCMN material.[28]

Analysis of the electrochemical impedance spectroscopy (EIS) data with an equivalent circuit model is helpful to understand in more detail the processes corresponding to the ASR value. Figure 9 shows the best fits of the EIS data to the equivalent circuit shown in the inset. R_1 represents the ohmic resistance from the electrolyte, whereas the ASR is represented by the sum of two resistances representing the electrode processes at high and low frequencies (ASR = $R_{HF} + R_{LF}$) with a parallel constant phase element (CPE) representing the effect of inhomogeneity. The resulting fitted parameters (including resistance, time constant and CPE exponent) in the temperature range 600−750 °C are listed in Table S5 of the Supporting Information. The R_1 electrolyte resistance fitted in Figure 9 yielded an ionic conductivity of 0.016 S cm^{-1} at 600 °C. At other points from 550 to 800 °C, the conductivity values obtained in this way are all in good agreement with reported values for SDC, suggesting the equivalent circuit proposed is correct.[29] Figure 10 shows the temperature dependence of the ASR ($R_{LF} + R_{HF}$) and the separate resistances of the LF (R_{LF}) and HF (R_{HF}) arcs of the BCMN electrode for the oxygen reduction reaction. The activation energies of the LF and HF arcs are found to be 147.9 and 112.1 kJ mol^{-1}, whereas that of the total cathode ASR is 130.0 kJ mol^{-1}.

Stability. To investigate the long-term stability of BCMN, we annealed the as-synthesized single-phase powders for an extended time (held at 750 °C for 240 h). For comparison, $Ba_{0.5}Sr_{0.5}Co_{0.8}Fe_{0.2}O_{3-\delta}$ (BSCF) powders (synthesized at 1100 °C/8 h and confirmed as single-phase by XRD) were also annealed under the same conditions. As shown in Figure 11, there are no significant changes in the

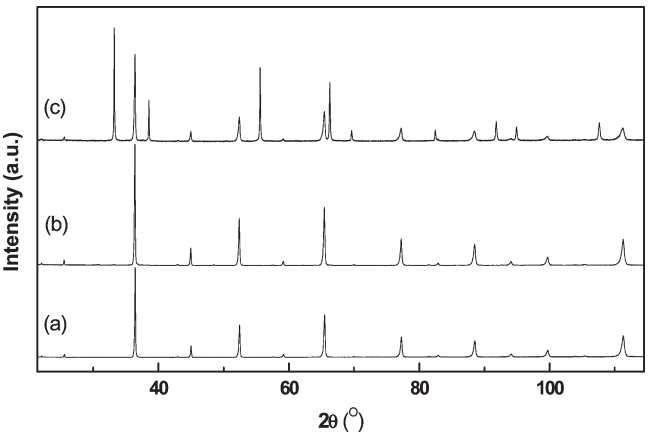

Figure 11. XRD patterns for $Ba_2CoMo_{0.5}Nb_{0.5}O_{6-\delta}$ (a) as-synthesized (1100 °C for 12 h), (b) after annealing in air at 750 °C/240 h, (c) $Ba_2CoMo_{0.5}Nb_{0.5}O_{6-\delta}$-SDC mixture after cofiring at 1050 °C/10 h.

XRD patterns before and after annealing observed for BCMN. The refined cell parameters with XRD data are 8.1117(1) and 8.1148(1) Å for the as-synthesized and annealed samples, respectively. In contrast, BSCF partially decomposes under the same conditions (see Figure S8 in the Supporting Information), suggesting improved long-term stability for this new material. The observations about the structural instability of BSCF agree well with previous studies, which show that BSCF separates into a mixture of the hexagonal phase of barium-rich iron-free cobalt perovskite, $(Ba_{0.75}Sr_{0.25})CoO_{3-\delta}$, and the cubic phase of strontium-rich, iron−cobalt perovskite, $(Ba_{0.25}Sr_{0.75})(Co_{0.6}Fe_{0.4})\ O_{3-\delta}$.[19,30,31]

For the specific SOFC cathode application of BCMN, the compatibility with the SDC electrolyte was also addressed. The reactivity tests between BCMN and SDC were carried out by cofiring a mixture of BCMN and SDC (weight ratio of 1:1) pressed pellet at different temperatures. Similarly, BSCF was also tested in comparison. As

(28) Li, S. Y.; Lu, Z.; Wei, B.; Huang, X. Q.; Miao, J. P.; Liu, Z. G.; Su, W. H. *J. Alloys Compd.* **2008**, *448*, 116.
(29) Eguchi, K.; Setoguchi, T.; Inoue, T.; Arai, H. *Solid State Ionics* **1992**, *52*, 165.
(30) Ovenstone, J.; Jung, J. I.; White, J. S.; Edwards, D. D.; Misture, S. T. *J. Solid State Chem.* **2008**, *181*, 576.
(31) Arnold, M.; Gesing, T. M.; Martynczuk, J.; Feldhoff, A. *Chem. Mater.* **2008**, *20*, 5851.

shown by the XRD data in Figure 11, no new phase is formed and no obvious peak shifts for either component were observed even after cofiring at 1050 °C for 10 h, an indication of the absence of solid-state reactions between SDC and BCMN. The refined cell parameters for BCMN and SDC after reaction are 8.1187(2) and 5.4314(1) Å (5.4288(5) Å for starting SDC sample). However, reaction of BSCF with SDC leads to obvious impurity phases produced even at a lower temperature, 1000 °C for 5 h (as shown in Figure S8 in the Supporting Information). This reaction between BSCF and SDC, along with its phase decomposition over time may partially explain the discrepancies in BSCF cathode properties from different authors corresponding to the spread in values reported earlier. Although no obvious reaction with SDC was observed for BCMN, the compositions of both cathode and electrolyte may change due to diffusion of the ions, as evidenced by XRD data in Figure 11 showing some peak broadening at 88.46 and 111.14° in (c) comparing with those of (b). EDX in the SEM indicated a slight interdiffusion of Co into SDC and Ce into BCMN on the interface (see Figure S9 in the Supporting Information).

Discussion

In the $A_2B'B''O_6$-type double perovskite structure, the arrangement of the B-cation sublattice is controlled primarily by the charge difference and secondarily by the size difference with a given A site.[32] The rock salt cation ordered arrangement is dominant when the charge difference is greater than two such as in the reported B site ordered Mo and Nb perovskites Sr_2FeMoO_6,[22] $Sr_2MgMoO_{6-\delta}$,[33] Ba_2LnNbO_6 (Ln = lanthanides and Y),[34] and $Sr_2Sr_{1-x}Nb_{1+x}O_{6-\delta}$.[35,36] The relevant ionic radii in the present case are $Co^{2+} = 0.745$ Å (high spin), $Co^{2+} = 0.65$ Å (low spin), $Mo^{6+} = 0.059$ nm, $Nb^{5+} = 0.064$ nm).[37] The present material is an Nb-doped variant of the rock-salt ordered Co^{2+} Ba_2CoMoO_6,[38] made by solid solution with the B-site disordered simple cubic Co^{3+} perovskite $BaCo_{0.5}Nb_{0.5}O_3$.[39] Although at the 1:1 ratio Co^{3+} and Nb^{5+} are disordered, the ordered domain sizes in the present BCMN material are large suggesting that the Co/Nb alternation is still favored, assigned to the presence of only 30% Co^{3+}, with the Co^{2+} charge state driving site order with Nb^{5+} owing to the larger charge difference. Co^{2+} and Nb^{5+} are ordered in the well-known 2:1 microwave dielectric perovskite $Ba_3CoNb_2O_9$; interestingly, in this class of ordered perovskite, dilution with a third cation of intermediate charge (Zr^{4+}) produces a transition to the 1:1 rock-salt type ordering of the type seen here.[40] In the present case, the rock-salt ordered 2+/6+ Ba_2CoMoO_6 is robust to the introduction of 50% of the lower charged cation Nb^{5+} on the Mo^{6+} site, where the common geometries adopted by d^0 cations may assist the tendency to retain order. The sizes of the ordered domains of over 60 nm from diffraction data are consistent with the sizes of the ordered regions observed in HRTEM and emphasize the robust nature of the B site ordering pattern despite the 50% substitutional cation disorder on one of the two sublattices.

The composition and structure of B-site ordered $Ba_2CoMo_{0.5}Nb_{0.5}O_{6-\delta}$ control both stability and properties. Instability against phase separation into hexagonal perovskites containing Co^{4+} is a problem for the Co^{4+}-containing cubic BSCF. The introduction of Mo^{VI} and Nb^{V} on half of the B sites strongly reduces the mean Co valence to just over two and thus suppresses the tendency for hexagonal stacking of the AO_3 layers, explaining the enhanced stability to thermal treatment and reactivity with the SDC electrolyte compared with BSCF. This is emphasized by the presence of hexagonal stacking faults (Figure 5) in the $x = 0.5$ material with a higher Co charge state of +3.5 − the stacking faults are completely suppressed at $x = 1$. This higher Co charge at $x = 0.25$ also reduces the drive to order the Co and Mo/Nb on both size and charge grounds, accounting for the simple cubic rather than rock-salt ordering observed here. The decreased Co charge state within the cubic structure does however negatively affect some of the key functions of the material as a cathode. The lower Co mean oxidation state considerably reduces the tendency to form anion vacancies, which are prevalent when the mean charge rises above +3 as in BSCF, and thus reduces the ionic component of the conductivity. The bonding with oxygen is necessarily less covalent for $Co^{2+/3+}$ in BCMN than in the higher oxidation state $Co^{3+/4+}$ present in BSCF, and this will reduce the electronic conductivity. A further contributor to the relatively low electronic conductivity of BCMN is the large (~8 Å) separation of the electronically active Co by intervening d^0 Mo centers imposed by the rock-salt ordering. The electronic conductivity is by hopping and presumably enhanced by the mixed valency at the Co site. The total conductivity of BCMN is thus more than 30 times lower than BSCF. As the performance of a fuel cell electrode depends on the ability to transport electrons and ions to the reactive site, it would be expected that the performance of BCMN would be markedly inferior to materials such as BSCF.

The literature shows the ASR for cathode materials depends strongly on the composition, morphology, and processing parameters. For example, at 600 °C, ASR values observed are 2.8 Ω cm^2 for $GdBaCo_2O_{5+\delta}$ (GBCO on YSZ), 1.15 Ω cm^2 for $La_{0.6}Sr_{0.4}CoO_{3-\delta}$ (LSC on SDC), 2.0 Ω cm^2 for $Sm_{0.5}Sr_{0.5}CoO_{3-\delta}$ (SSC on SDC), 1.3 Ω cm^2 for $La_{0.6}Sr_{0.4}Co_{0.2}Fe_{0.8}O_{3-\delta}$ (LSCF on $Gd_{0.1}Ce_{0.9}O_{1.95}$), and 0.1−1.1 Ω cm^2 for $Ba_{0.5}Sr_{0.5}Co_{0.8}Fe_{0.2}O_{3-\delta}$

(32) Anderson, M. T.; Greenwood, K. B.; Taylor, G. A.; Poeppelmeier, K. R. *Prog. Solid State. Chem.* **1993**, *22*, 197.
(33) Bernuy-Lopez, C.; Allix, M.; Bridges, C. A.; Claridge, J. B.; Rosseinsky, M. J. *Chem. Mater.* **2007**, *19*, 1035.
(34) Fu, W. T.; IJdo, D. J. W. *J. Solid State Chem.* **2006**, *179*, 1022.
(35) Glöckner, R.; Neiman, A.; Larring, Y.; Norby, T. *Solid State Ionics* **1999**, *125*, 369.
(36) Li, M. R.; Hong, S. T. *Chem. Mater.* **2008**, *20*, 2736.
(37) Shannon, R. D. *Acta Crystallogr., Sect. A* **1976**, *32*, 751.
(38) Martínez-Lope, M. J; Alonso, J. A.; Casais, M. T.; Fernández-Díaz, M. T. *Eur. J. Inorg. Chem.* **2002**, *9*, 2463.
(39) Yoshii, K. *J. Solid. State. Chem.* **2000**, *151*, 294.
(40) Davies, P. K.; Wu, H.; Borisevich, A. Y.; Molodetsky, I. E.; Farber, L. *Annu. Rev. Mater. Res.* **2008**, *38*, 369.

(BSCF, on SDC).[8,41,44] The direct comparison with the same processing parameters here gives BCMN an ASR 2.5 times higher than BSCF. Therefore, despite the relatively low total conductivity, the ASR data indicate the BCMN performance is comparable to that of other cathodes such as LSM and BSCF.

The ASR activation energy of 130 kJ mol^{-1} for the oxygen reduction reaction on the BCMN cathode is comparable to that of BSCF (116−127.4 kJ mol^{-1}) and LSCF (131−138 kJ mol^{-1}) on the SDC electrolyte in the same temperature range.[7,45] ASR is decomposed into two separate high- and low-frequency processes, as shown in Table S5 of the Supporting Information and Figure 8. Considering the LF arc, the capacitance 1.1×10^{-2} to 5.7×10^{-2} F cm^{-2}, and the time constant values ($\tau = RC$) 8.6×10^{-3} to 2.3×10^{-3} s at 650−750 °C, together with the high activation energy of 147.9 kJ mol^{-1} are consistent with the characteristics associated with the dissociative adsorption and diffusion of oxygen on the surface of the electrode, i.e., with surface kinetic impedance. The capacitance value is comparable to that of the dense LSCF microelectrode 15×10^{-3} F cm^{-2} (750 °C), and the porous LSCF (3.6×10^{-3} F cm^{-2}), LSM (12.2×10^{-3} Ω^{-1} cm^{-2} s^n, $n = 0.7$, 700 °C), and $La_{0.74}Ca_{0.25}Co_{0.8}Fe_{0.2}O_{3-\delta}$ (12.7×10^{-3} Ω^{-1} cm^{-2} s^n, $n = 0.89$, 750 °C) electrodes.[46−49]

The HF arc has a capacitance 1 order of magnitude lower than that of the LF arc and a typical time constant $\sim 1 \times 10^{-4}$ s. This is likely related to the charge-transfer process of reduction from O to O^{2-}, as suggested by prior studies on LSCF and LSC cathodes.[50−52] For the present BCMN material, the rate-limiting steps are the dissociative adsorption and diffusion at the BCMN electrode surface (i.e., the process in the LF arc) at low temperatures and the charge transfer process at high temperature when $T > 700$ °C. As shown in Figure 8 and Table S5 in the Supporting Information, BCMN has $R_{LF} = 0.78$ Ω cm^2 and $R_{HF} = 0.55$ Ω cm^2 at 600 °C, indicating a comparable contribution from surface kinetic impedance (R_{LF}) and charge-transfer impedance (R_{HF}). In contrast, R_{LF} has been found to be the predominant contribution to the ASR of materials such as LSC and LSCF. For example, values of $R_{LF} = 3.0$ Ω cm^2 and $R_{HF} = 1.0$ Ω cm^2 were reported for an LSCF electrode at 590 °C, and $R_{LF} = 1.6$ Ω cm^2 and $R_{HF} = 1.1$ Ω cm^2 for an LSC-SDC composite cathode.[52,53] As BCMN has limited electrical conductivity (1.2 and 1.0 S/cm at 800 and 700 °C, respectively, compared to 300−320 S/cm for LSCF and LSM at 750 °C[9,47] the enhanced surface kinetics of the present material may play an important role in the surprisingly good electrode performance found here for the oxygen reduction reaction (i.e., the low ASR values comparable to the existing materials with much higher intrinsic total conductivities). This suggests that the inclusion of Mo in the material assists the electrochemical oxygen reduction via catalytic promotion of the dissociation and surface diffusion of oxygen species on the cathode to the three-phase boundary (TPB).[19,20,54] This inference is supported by the activation energy for the oxygen surface exchange involving the dissociative adsorption and diffusion of oxygen on the surface of the electrode seen in the LF arc found for the BCMN electrode, ~147.9 kJ mol^{-1}, which is lower than that of the porous LSM (202−236 kJ mol^{-1}) the dense LSCF microelectrode (154.4 kJ mol^{-1}), and the dense BSCF microelectrode 173.7 kJ mol^{-1} over the temperature range 600−750 °C.[47,48,55] The known ability of Mo^{VI} to enhance dioxygen dissociation in hydrocarbon oxidation catalysis may thus be an important factor in the cathode behavior of BCMN. BCMN is also expected to display oxide ion conductivity because of the oxygen vacancies, though these are less abundant than in BSCF.

Conclusion

The new oxide, $Ba_2CoMo_{0.5}Nb_{0.5}O_{6-\delta}$ (BCMN), with a B-site cation ordered double perovskite structure in which d^0 Mo^{VI} is separated from the *d*-electron bearing Co, exhibits comparable electrochemical properties and improved stability compared with some existing candidate SOFC cathode oxides. The role of Mo in dioxygen activation, possibly through the LF process corresponding to dioxygen cleavage and surface motion to the reduction site, offsets the reduction produced by the introduction of d^0 Mo(VI) in electronic and ionic conductivity, and can be proposed as the origin of the cathode performance of BCMN.

Acknowledgment. We thank EPSRC for support under EP/C511794 and for access to ISIS, where Dr. R. I. Smith is thanked for assistance on the POLARIS instrument.

Supporting Information Available: Additional figures and tables (PDF). This material is available free of charge via the Internet at http://pubs.acs.org.

(41) Tarancón, A.; Morata, A.; Dezanneau, G.; Skinner, S. J.; Kilner, J. A.; Estradé, S.; Hernández-Ramírez, F.; Peiró, F.; Morante, J. R. *J. Power Sources* **2007**, *174*, 255.
(42) Bellino, M. G.; Sacanell, J. G.; Lamas, D. G.; Leyva, A. G.; de Reca, N. E. W. *J. Am. Chem. Soc.* **2007**, *129*, 3066.
(43) Grunbaum, N.; Dessemond, L.; Fouletier, J.; Prado, F.; Caneiro, A. *Solid State Ionics* **2006**, *177*, 907.
(44) Sahibzada, M.; Benson, S. J.; Rudkin, R. A.; Kilner, J. A. *Solid State Ionics* **1998**, *113−115*, 285.
(45) Esquirol, A.; Kilner, J. A.; Brandon, N. P. *Solid State Ionics* **2004**, *175*, 63.
(46) Baumann, F. S.; Fleig, J.; Habermeier, H. U.; Maier, J. *Solid State Ionics* **2006**, *177*, 1071.
(47) Jiang, S. P. *Solid State Ionics* **2002**, *146*, 1.
(48) Jiang, S. P.; Love, J. G.; Ramprakash, Y. *J. Power Sources* **2002**, *110*, 201.
(49) Chen, C. W.; Tsai, D. S.; Jin, T. Y.; Chung, W. H.; Chou, C. C. *Solid State Ionics* **2008**, *179*, 330.
(50) Adler, S. B.; Lane, J. A.; Steele, B. C. H. *J. Electrochem. Soc.* **1996**, *143*, 3554.
(51) Shah, M.; Barnett, S. A. *Solid State Ionics* **2008**, *179*, 2059.
(52) Dusastre, V.; Kilner, J. A. *Solid State Ionics* **1999**, *126*, 163.
(53) Zhao, F.; Peng, R. R.; Xia, C. R. *Mater. Res. Bull.* **2008**, *43*, 370.
(54) Baumann, F. S.; Fleig, J.; Cristiani, G.; Stuhlhofer, B.; Habermeier, H. U.; Maier, J. *J. Electrochem. Soc.* **2007**, *154*, B931.
(55) Fleig, J. *Annu. Rev. Mater. Res.* **2003**, *33*, 361.